J. Chem. Sci. Vol. 127, No. 8, August 2015, pp. 1347–1360.
DOI 10.1007/s12039-015-0897-8

Investigation of physicochemical properties and catalytic activity of nanostructured $Ce_{0.7}M_{0.3}O_{2-\delta}$ (M = Mn, Fe, Co) solid solutions for CO oxidation

P VENKATASWAMY[a], D JAMPAIAH[a], C U ANIZ[b] and BENJARAM M REDDY[a,*]

[a]Inorganic and Physical Chemistry Division, CSIR–Indian Institute of Chemical Technology, Uppal Road, Hyderabad 500 007, India

[b]R&D Division, Sud–Chemie India Pvt. Limited, Binanipuram, Kerala 683 502, India

e-mail: bmreddy@iict.res.in; mreddyb@yahoo.com

MS received 13 January 2015; revised 24 March 2015; accepted 23 April 2015

Abstract. In this work, nanosized $Ce_{0.7}M_{0.3}O_{2-\delta}$ (M = Mn, Fe, Co) solid solutions were prepared by a facile coprecipitation method and evaluated for CO oxidation. The physicochemical properties of the synthesized samples were investigated by various characterization techniques, namely, XRD, ICP-OES, BET surface area, SEM-EDX, TEM and HRTEM, Raman, XPS, and H_2-TPR. XRD studies confirmed the formation of nanocrystalline single phase $Ce_{0.7}M_{0.3}O_{2-\delta}$ solid solutions. ICP-OES analysis confirmed actual amount of metal loadings in the respective catalysts. The BET surface area of $Ce_{0.7}M_{0.3}O_{2-\delta}$ samples significantly enhanced after the incorporation of dopants. TEM studies confirmed nanosized nature of the samples and the average particle sizes of $Ce_{0.7}M_{0.3}O_{2-\delta}$ were found to be in the range of ~8–16 nm. Raman studies indicated that the incorporation of dopant ions into the CeO_2 lattice promote the formation of more oxygen vacancies. The existence of oxygen vacancies and different oxidation states (Ce^{3+}/Ce^{4+} and Mn^{2+}/Mn^{3+}, Fe^{2+}/Fe^{3+}, and Co^{2+}/Co^{3+}) in the doped CeO_2 samples were further confirmed from XPS investigation. TPR measurements revealed an enhanced reducibility of ceria after the incorporation of dopants. The catalytic activity results indicated that the doped CeO_2 samples show excellent CO oxidation activity and the order of activity was found to be $Ce_{0.7}Mn_{0.3}O_{2-\delta} > Ce_{0.7}Fe_{0.3}O_{2-\delta} > Ce_{0.7}Co_{0.3}O_{2-\delta} > CeO_2$. The superior CO oxidation performance of CeO_2-MnO_x has been attributed to a unique Ce-Mn synergistic interaction, which facilitates materials with promoted redox properties and improved oxidation activity.

Keywords. CeO_2; metal-doping; nanosized solid solution; synergistic interaction; Redox properties; CO oxidation.

1. Introduction

Stringent environmental regulations are in force to mitigate air pollution and greenhouse gas (GHG) emissions because they pose serious threats to human health and the environment across the world. Among various emitted toxic pollutants, carbon monoxide (CO) is one of the major pollutants and it is a global malady causing innumerable irreversible changes to our planet.[1] It also contributes indirectly to global warming and ozone depletion. The progressive increase of CO emissions into the environment as a result of incomplete combustion of fossil fuels can lead to harmful health effects by reducing oxygen delivery to the body's organs (like the heart and brain) and tissues.[2] Therefore, various options must be undertaken to combat against the problems arising due to emission of CO. The catalytic oxidation is a more energy-efficient and environmentally friendly technology for CO abatement.[3] For wide implementation of catalytic oxidation, thermally, mechanically, and chemically stable catalysts are required. Various catalysts such as metal oxides, mixed metal oxides, supported systems, and pervoskites[3–6] have been examined extensively for CO oxidation reaction. In particular, noble metal catalysts such as supported Pd and Pt, exhibit an excellent catalytic performance. Nevertheless, the high cost of noble metals and their sensitivity to sulphur poisoning have limited their industrial application.[7]

Over the last decades, an intense research activity has been devoted to search for inexpensive catalysts to replace the noble metals for catalytic oxidation of CO. Cerium oxide is one of the most important rare earth oxides due to its intrinsic chemical properties such as high oxygen storage capacity (OSC) and high oxygen mobility, which originate from variable valence states (+3 and +4) of cerium ion.[8] As a result, it is widely used in various catalytic applications such as three-way

*For correspondence

catalysis (TWCs), water-gas shift reaction, solid oxide fuel cells, and oxygen sensors. The oxygen storage and release in ceria is favoured by its unique fluorite structure. However, while using ceria-based materials in TWCs, the major concern is about the thermal stability of ceria (CeO_2) component at higher temperatures (∼1200 K). At such high operating temperatures, the OSC of ceria significantly decreases upon thermal aging due to the growth of ceria crystallite size, thereby losing the active surface area. The increase in crystallite growth and thermal sintering process occurs due to the mass transport at an atomic scale caused by a concentration gradient set at higher temperatures.[9,10] Therefore, improving thermal stability of pure CeO_2 is an important task to exploit this material successfully in several applications. Many attempts have been made to enhance the thermal stability of CeO_2 such as controlling the crystal morphology and size, modifying the surface property, and metal doping.[11,12] Among these modifications, doping with lower valent cations is one of the most effective and readily realized options.[13] The metal doping can improve the oxygen storage capacity, diffusivity, and redox properties due to the formation of structural defects in the ceria lattice.[9] Therefore, there is a strong demand for the development of doped ceria materials with low cost and relatively high activity.

In recent years, ceria-based materials with doped transition metal oxides have attracted much attention, owing to their high thermal stability, design flexibility and low-cost.[14] Particularly, the base metal oxide catalysts like Mn, Fe, and Co were mostly exploited since they exhibit different oxidation states and excellent redox properties.[15] It was clearly demonstrated that the doping of these multivalent ions produce lattice defects and oxygen vacancies with the formation of a ceria-based solid solution structure, thereby increase the reducibility of ceria at low temperatures.[16,17] These defects and vacancies provide major transport channels for surface oxygen (O_2^-, O^-), lattice oxygen (O_2^-) and facilitate high catalytic activity at lower temperatures.[18] Since the OSC and redox properties are very important in catalytic applications, an investigation on the influence of structural features of CeO_2–MO_x mixed oxides was undertaken.[19,20] Therefore, the aim of the present work was to investigate the structural and surface modifications of cerium oxide doped with three different transition metals (Mn, Fe, Co) and their application for CO oxidation reaction. Accordingly, the $Ce_{0.7}M_{0.3}O_{2-\delta}$ (M = Mn, Fe, Co) solid solutions were synthesized by a co-precipitation method and the physicochemical properties were evaluated using X-ray diffraction (XRD), inductively coupled plasma-optical emission spectroscopy (ICP-OES), Brunauer–Emmett–Tellerv (BET) surface area, scanning electron microscopy-energy dispersive X-ray analysis (SEM-EDX), transmission electron microscopy (TEM), high resolution transmission electron microscopy (HRTEM), Raman spectroscopy (RS), X-ray photoelectron spectroscopy (XPS), and H_2-temperature programmed reduction (H_2-TPR) measurements.

2. Experimental

2.1 *Catalyst preparation*

A simple co-precipitation method was employed for the preparation of nanosized $Ce_{0.7}M_{0.3}O_{2-\delta}$ (M = Mn, Fe, Co; Ce/M 70:30 mol% based on oxides) solid solutions. In this synthesis, cerium(III) nitrate hexahydrate (Aldrich, AR grade), manganese(II) nitrate tetrahydrate (Merck, AR grade), iron(III) nitrate nonahydrate (Aldrich, AR grade), and cobalt(II) nitrate hexahydrate (Aldrich, AR grade) were used as the cerium, manganese, iron, and cobalt precursors, respectively. A dilute aqueous ammonia solution was used to hydrolyze the metal salt precursors at a certain solution pH (∼8.5). In order to prepare $Ce_{0.7}Mn_{0.3}O_{2-\delta}$, the desired amounts of Ce and Mn nitrate precursors were dissolved separately in distilled water and mixed together under vigorous stirring conditions until the clear solution is formed. An aqueous ammonia solution was added gradually drop-wise with vigorous stirring to reach the pH value ∼8.5. Subsequently, the mixed solution was stirred continuously for 24 h to complete the reaction. After that, the precursor precipitate was separated from the supernatant by vacuum filtration and washed several times with distilled water until free from anion impurities. The obtained precipitates were then dried in an electrical oven at 373 K for 12 h. The oven dried sample was crushed using an agate mortar and calcined at 773 K for 5 h in a closed electric furnace at a heating rate of 5 K min^{-1} to obtain nanocrystalline form of $Ce_{0.7}Mn_{0.3}O_{2-\delta}$ solid solution. A similar method was followed to prepare $Ce_{0.7}Fe_{0.3}O_{2-\delta}$, and $Ce_{0.7}Co_{0.3}O_{2-\delta}$ using the respective nitrate precursors. Pure CeO_2 sample was also synthesized by the same procedure for comparative purposes. The prepared samples were designated as pure CeO_2 (C), $Ce_{0.7}Mn_{0.3}O_{2-\delta}$ (CM), $Ce_{0.7}Fe_{0.3}O_{2-\delta}$ (CF), and $Ce_{0.7}Co_{0.3}O_{2-\delta}$ (CC), respectively.

2.2 *Catalyst characterization*

X-ray powder diffraction patterns were acquired on an X'pert Pro MPD powder diffractometer (PANalytical Company) equipped with a nickel-filtered Cu Kα (0.15418 nm) radiation source and a scintillation counter detector (SCD). The scattered intensity data

were collected from 2θ values of 2 to 80° by scanning at 0.01° steps with a counting time of 1 s at each step. Crystalline phases were identified by matching with the International Centre for Diffraction Data Powder Diffraction File (ICDD-PDF). The average crystallite size (D_{XRD}) of the samples was determined with the help of Debye-Scherrer equation from line broadening and the lattice parameters (a) were estimated by a standard cubic indexation method using the intensity of the most prominent peak (111).

The chemical analysis of the prepared samples was performed by inductively coupled plasma optical emission spectroscopy (ICP-OES, Thermo Jarrel Ash model IRIS Intrepid II XDL, USA) to confirm the respective concentrations of the elements in the catalyst. For ICP analysis, approximately 50 mg of the sample was dissolved in a solution of 25 mL aqua regia and 475 mL distilled water. Then 10 mL of the above solution was diluted to 250 mL.

The surface area and pore size distribution of the as-prepared samples were determined by N_2 adsorption-desorption isotherms at liquid N_2 temperature (77 K) on a Micromeritics (ASAP 2000) analyzer. Specific surface area and pore size distribution were calculated by BET and Barrett-Joyner-Halenda (BJH) methods, respectively. Prior to the measurements, the samples were pre-treated in a vacuum oven at 473 K for 2 h to remove any residual moisture.

SEM studies were performed by using a Zeiss EVO® series electron microscope to examine surface morphology, and the energy dispersive X-ray analysis (EDX) was used to determine the elemental composition of samples. The scanning electron microscope was equipped with a LaB_6 source and an EDAX/DX4 detector. The acceleration potential voltage was maintained at 15 kV and samples were metallised with gold.

The TEM-HRTEM studies were made on a TECNAIG2 TEM microscope equipped with a slow-scan CCD camera and at an accelerating voltage of 200 kV. Samples for TEM analysis were prepared by crushing the materials in an agate mortar and dispersing ultrasonically in ethyl alcohol. After well dispersion, a droplet was deposited on a copper grid supporting a perforated carbon film and allowed to dry. The specimen was examined under vacuum at room temperature.

Raman spectra were obtained at room temperature on a Horiba Jobin-Yvon HR 800 Raman spectrometer fitted with a confocal microscope and liquid-nitrogen cooled charge-coupled device (CCD) detector. The laser line at 632 nm of Ar^+ ion (Spectra Physics) was used as an excitation source for the visible Raman spectroscopy. The laser was focused on the sample under a microscope with the diameter of the analyzed spot being $\sim$1 μm. The acquisition time was adjusted according to the intensity of Raman scattering. The wavenumber values reported from the spectra are accurate to within 2 cm^{-1}.

XPS analyses were performed using a PHI 5000 Versa probe (Ulvac-PHI) Spectrometer. The X-ray source utilized was the Mg Kα (1253.6 eV) radiation. The analysis was done at room temperature and the pressures were typically on the order of less than 10^{-8} Pa. The charging of samples was corrected by setting the binding energy of the adventitious carbon (C 1s) at 284.5 eV. The samples were out gassed overnight in a vacuum oven at 283 K before XPS measurements. All binding energies were measured within a precision of $\pm$ 0.3 eV.

The TPR analysis was used for evaluating the reduction properties of the prepared catalysts and was obtained on an automated Micromeritics AutoChem II-2720 instrument equipped with a thermal conductivity detector (TCD). Approximately 30 mg of the sample mass was placed on the top of quartz wool in a U-shaped quartz reactor (Inner diameter 5 mm). Sample was pre-treated at a rate of 10 K min^{-1} to 473 K under a pure He gas at a flow rate of 30 mL min^{-1} for 30 min to clean the surface of the catalysts before TPR investigation. After cooling down to room temperature, introducing the reduction agent of 5 vol% H_2/Ar with a flow rate of 20 mL min^{-1}, the temperature was programmatically raised to 1073 K at a ramp of 5 K min^{-1}, keeping all the parameters unchanged. The outlet of the reactor was connected to a cold trap to absorb the water molecules resulted by the reduction of the catalysts.

2.3 *Catalytic activity measurements*

The activity of the catalysts for the oxidation of CO was measured in the temperature range of 300–773 K at normal atmospheric pressure using a fixed-bed microreactor at a heating ramp of 5 K min^{-1}. The samples (approximately 100 mg, particle size = 250–350 μm) were placed in the reactor (2 mm inner diameter and length 250 mm) and diluted with quartz particles with the same particle size, in order to keep a constant volume and better temperature control in the catalytic bed. The reaction temperature was monitored and controlled by using a thermocouple inserted into the middle of catalyst bed. The following gases and gas mixtures were used (supplied by Air Liquid): argon (> 99.99% purity), 9.98% CO (> 99.99% purity), and 10.2% O_2 (> 99.99% purity) with argon as balance. The CO/O_2 reactant feed ratio was 1 and the partial pressures of CO and O_2 were in the range of 10 mbar. The total gas flow rates were guarded by using three mass flow controllers in the

range of 50–60 N mL min^{-1} (milliliters normalized to 273.15 K and 1 atm.). The CO and CO_2 gas concentrations were measured using an Uras 14 infrared analyzer module, and the O_2 concentration was measured using a Magnos 16 analyzer (Hartmann & Braun). Prior to the oxidation of CO, the catalyst was heated to 773 K in a 10.2% O_2/Ar gas mixture, with a heating ramp of 10 K min^{-1}, and kept at the final temperature for 1 h. The oxidized sample was then purged with Argon to avoid gas phase reaction and cooled to the desired starting temper ature. The CO/O_2 reactant feed ratio was 1 and the partial pressures of CO and O_2 were in the range of 10 mbar.

3. Results and Discussion

3.1 *Characterization studies*

The crystallinity and phase analysis of the prepared mixed oxides were studied by X-ray powder diffraction analysis. Figure 1a shows the XRD patterns of CeO_2–MO_x (M = Mn, Fe, Co) samples along with pure ceria calcined at 773 K. As can be clearly observed that all the diffraction peaks could be attributed to ceria with a cubic fluorite structure (JCPDS No. 34-0394).[21] No diffraction peaks corresponding to MO_x related oxide phases or any other impurity phases are detected in the mixed oxides. However, a shift to higher diffraction angles can be observed (figure 1b) for all doped samples compared with that of pure CeO_2. It can be ascribed to the introduction of dopants into the ceria lattice, which resulted in the formation of $Ce_{0.7}M_{0.3}O_{2-\delta}$ solid solutions as reported in earlier studies.[16,22] The lattice parameter (a) values corresponding to the cubic phase have been calculated for samples and shown in table 1. It is evident that the lattice parameters of the mixed oxides are found to be slightly smaller than those of pure ceria. This could be due to the smaller ionic radius of respective dopant ions Mn^{x+} (Mn^{2+} = 0.083 nm; Mn^{3+} = 0.065 nm), Fe^{x+} (Fe^{2+} = 0.074 nm; Fe^{3+} = 0.064 nm), and Co^{x+} (Co^{2+} = 0.078 nm; Co^{3+} = 0.063 nm) when compared to Ce^{4+} = 0.097 nm.[22–24] Furthermore, as shown in figure 1a, the diffraction peaks of CeO_2–MO_x mixed oxides are lower in intensity and broader than the pure ceria. The observed peak broadening in the XRD patterns of doped ceria samples can be interpreted in terms of crystallite size and lattice strain. Accordingly, the crystallite size (D_{XRD}) of the samples was calculated by using the Debye–Scherer equation considering full-width at half-maxima (FWHM) of the most intense (111) peak of fluorite structure. The procedure for calculation of crystallite sizes for various samples using the above equation is shown in table S1 (supporting information) and the obtained results are presented in table 1. These values reveal that the dopant cations exhibited a strong influence on the lowering of crystallite size of the pure ceria. Interestingly, the influence of Mn ions on ceria crystallite size was much more effective than that of Fe and Co ions. The crystallite size of the mixed oxides followed the order CM > CF > CC >C, which is in line with BET surface area results. Further, the smaller crystallite sizes can be attributed to the presence of more crystal defects, which are very important for catalytic oxidation reactions. According to Choudary *et al*., oxygen defects

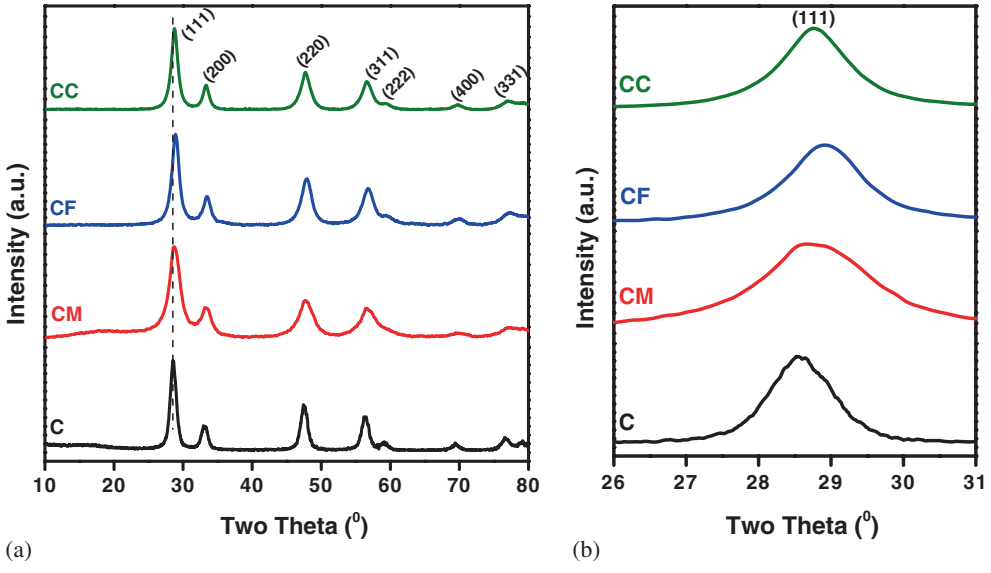

Figure 1. (a) Powder X-ray diffraction patterns of pure CeO_2(C), $Ce_{0.7}Mn_{0.3}O_{2-\delta}$(CM), $Ce_{0.7}Fe_{0.3}O_{2-\delta}$ (CF), and $Ce_{0.7}Co_{0.3}O_{2-\delta}$ (CC) samples calcined at 773 K; (b) enlarged view of selected 2θ region.

Table 1. BET surface area, average pore size, pore volume, crystallite size, lattice parameter, lattice strain, particle size and A_{Vo}/A_{F2g} ratio of pure CeO_2(C), $Ce_{0.7}Mn_{0.3}O_{2-\delta}$(CM), $Ce_{0.7}Fe_{0.3}O_{2-\delta}$ (CF), and $Ce_{0.7}Co_{0.3}O_{2-\delta}$(CC) samples calcined at 773 K.

Sample	SA (m^2g^{-1})	Average pore size (nm)	Pore volume (cm^3g^{-1})	D (nm)	LP (Å)	ε[a]	D_{BET} A_{Vo}/A_{F2g}(nm)
C	41	3.96	0.04	8.92	5.41	0.041	20.28 0.18
CM	58	30.1	0.44	7.19	5.35	0.068	14.33 0.46
CF	55	34.8	0.41	7.11	5.34	0.061	15.12 0.28
CC	51	39.7	0.38	8.41	5.39	0.054	16.31 0.24

[a]Calculated from Williamson–Hall plots.

and generation of Ce^{3+} ions in the fluorite structure mainly contribute to the lattice strain in CeO_2.[25] This can occur when the lower valent cations are introduced into the ceria lattice.[26] Therefore, in order to elucidate the affect of dopants on the ceria fluorite structure, we have determined the magnitude of lattice strain (ε), present in each of the sample, using Williamson-Hall (We-H) plot. For the calculation of strain, $\beta Cos\theta/\lambda$ is plotted against $Sin\theta/\lambda$ and the plotted points are linearly fitted. The slope of the fitting gives the value of lattice strain. The corresponding graphs and the values are shown in figure S1 (supporting information) and in table 1, respectively. It can be clear seen that the lattice strain in pure ceria increased with the doping of transition metal ions. Generally, the difference in the radii of the host and guest ions can be reasoned to produce oxygen vacancies in the lattice to maintain charge balance. These lattice site oxygen vacancies also generate more strain in the lattice of doped samples. Among the doped samples, the CM sample exhibited more lattice strain over pure CeO_2. In addition, the chemical analysis of the CeO_2–MO_x mixed oxides are also determined by ICP-OES analysis and the results are shown in table S2 (supporting information). It is confirmed that the molar ratios of cerium ion and dopant ions in the $Ce_{0.7}M_{0.3}O_{2-\delta}$ solid solutions are in accordance with the nominal compositions, indicating the good stoichiometric homogeneity of cerium ions and dopant ions in the synthesized samples. Therefore, the stoichiometry and the chemical formulae expected from the results can be represented as $Ce_{0.69}Mn_{0.31}O_{2-\delta}$, $Ce_{0.69}Fe_{0.31}O_{2-\delta}$, and $Ce_{0.69}Co_{0.31}O_{2-\delta}$ for CeO_2–MnO_x, CeO_2–FeO_x, and CeO_2–CoO_x mixed oxides, respectively.

The N_2 adsorption–desorption isotherms of the C, CM, CF, and CC samples calcined at 773 K are shown in figures 2a, 2b, 2c and 2d, respectively. It could be seen from the figures that all samples exhibited type IV adsorption isotherms as defined by IUPAC.[27] A close look at the isotherms reveals that there is much less adsorption in the low pressure region and the hysteresis loop is almost like an H3 isotherm. This may be attributed to the so called pore blocking or percolation effect.[28] This effect is expected to occur when the pore has access to the external surface only through a narrower neck as in an ink bottle pore. A distinct capillary condensation step at a relative pressure in the range of 0.55–0.98 indicates that uniformly sized pores are generated after the two steps replication process. Further, as observed in the case of CM, CF and CC samples, the porous network is different in each case because of surface heterogeneity and varying particle size relatively. As indicated by narrow hysteresis loops with steep and nearly parallel adsorption and desorption branches, the samples studied in this work appear to have good pore connectivity and relatively narrow pore size distribution. The pore size distribution for the prepared samples, which are calculated from the desorption branches of isotherms using the BJH method are shown in figure 2 (inset view). The CM, CF, CC, and pure CeO_2 samples showed average pore size of 30.1, 34.8, 39.7, and 3.96 nm, respectively, which confirm the mesoporous nature of the catalysts. It can be concluded that each sample exhibits unimodal pore size distribution. The specific BET surface area, pore size and pore volumes of these catalysts are also summarized in table 1. It is clear that the specific surface area and pore volumes were increased after the incorporation of dopants into the ceria lattice. These changes may be related to the grain size of the samples to some extent. In other words, the incorporation of transition metal dopants into the lattice of CeO_2 could improve the texture property effectively. Furthermore, the relatively high specific surface area of the doped samples can also be associated to the nanometric size of the particles.

The average particle size values of all samples are also calculated from the surface area measurement using the equation $D_{BET} = 6000/(S_{BET} \times \rho_{CeO2})$, where D_{BET} the average particle size (nm), S_{BET} (m^2/g) is BET surface area and ρ (g/cm^3) is the theoretical density of the ceria ($\sim$7.215 g/cm^3), assuming that particles are smooth spheres. The obtained analysis results are shown in table 1. In general, the crystallite size (D_{XRD}) is not equal to the actual particle size (D_{BET}) due to agglomeration effects in the latter.[29] It can be clearly

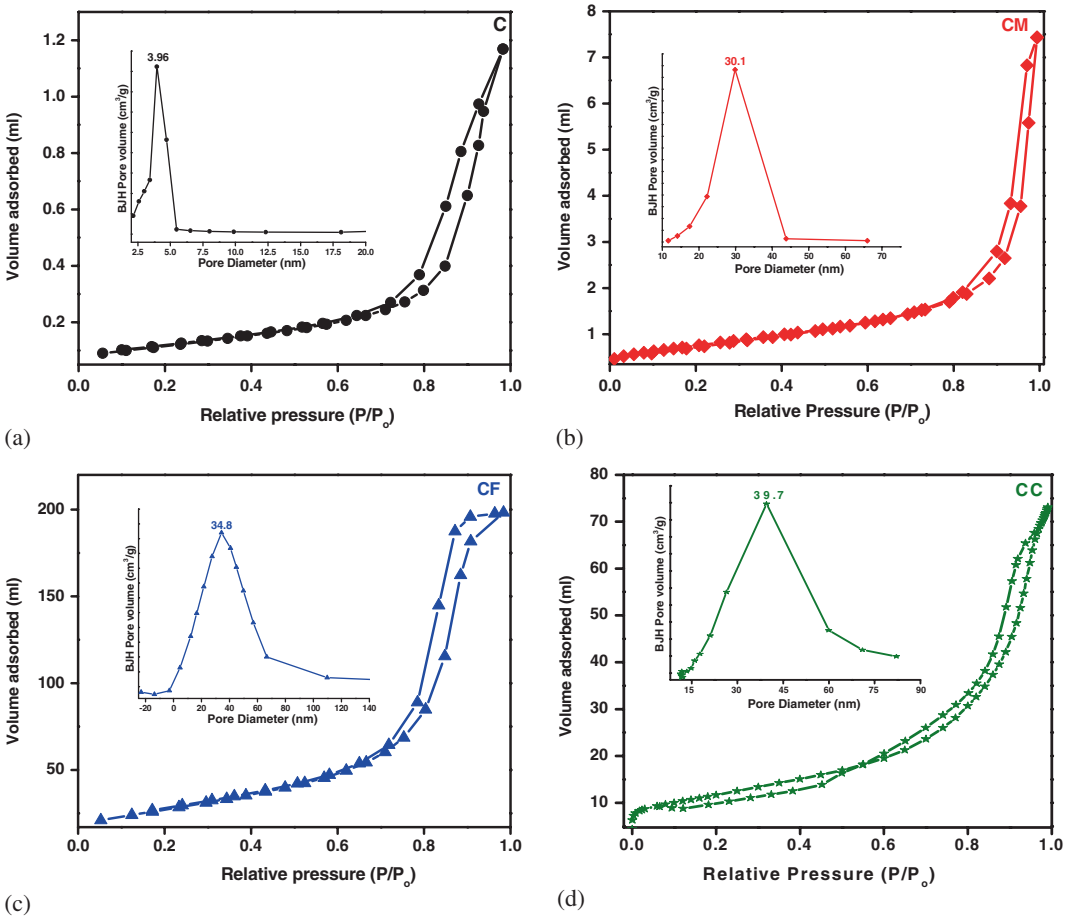

Figure 2. N_2 adsorption-desorption isotherms of (a) pure CeO_2(C); (b) $Ce_{0.7}Mn_{0.3}O_{2-\delta}$ (CM); (c) $Ce_{0.7}Fe_{0.3}O_{2-\delta}$ (CF); and (d) $Ce_{0.7}Co_{0.3}O_{2-\delta}$(CC) samples calcined at 773 K (inset: pore size distribution curves).

seen from table 1 that for any particular sample, the values of average particle size is slightly higher than that of average crystallite size. However, in the case of pure ceria the difference is very high, due to higher particle agglomeration of crystalline nanoparticles. On the other hand, the particle size values of CM, CF, and CC samples are closely consistent with the observations made by TEM analysis, which are discussed in the later sections.

In order to investigate the surface morphology of the synthesized $Ce_{0.7}Mn_{0.3}O_{2-\delta}$(CM) solid solutions (selected one), SEM studies were performed and the obtained image is shown in figure 3a. The CM sample clearly shows the nanoparticle morphology and a little agglomeration of the primary nanoparticles.[21] In general the composition can be very sensitive for the catalytic applications. Therefore the elemental composition of CM sample was assessed by EDX analysis and the results are mentioned in figure 3b. In EDX spectrum, numerous well-defined peaks are evident, which can be related to Mn, O and Ce and they clearly support that the synthesized sample is made of Mn, O and Ce with the composition as per the initial precursor concentrations. No other peaks related to impurities were detected in the spectrum indicating that nitrate ions were completely removed during the washing. Further, this investigation also gave evidence that the Mn dopant is homogeneously distributed in the matrix of CeO_2.

The morphology and microstructure of CM, CF, and CC samples are further illustrated by TEM and HRTEM analysis. Typical TEM images of Mn, Fe, and Co-doped ceria samples are shown in figures 4a, 4c, and 4e, respec tively. It is clearly observed from the TEM micrographs that in all catalysts the nanosized particles are homogeneously distributed with the spherical morphology along the surface. The average particle size values of the Mn, Fe, and Co-doped ceria samples were found to be in the range of ∼8–10, 11–13, and 14–16 nm, respectively, which are in good agreement with the calculated average particle sizes from BET analysis as shown in table 1. Besides, HRTEM was also employed to obtain the internal structure of the produced nanoparticles. Distinct lattice planes in HRTEM images (4b, 4d, and 4f) of all the samples are demonstrating a high degree of

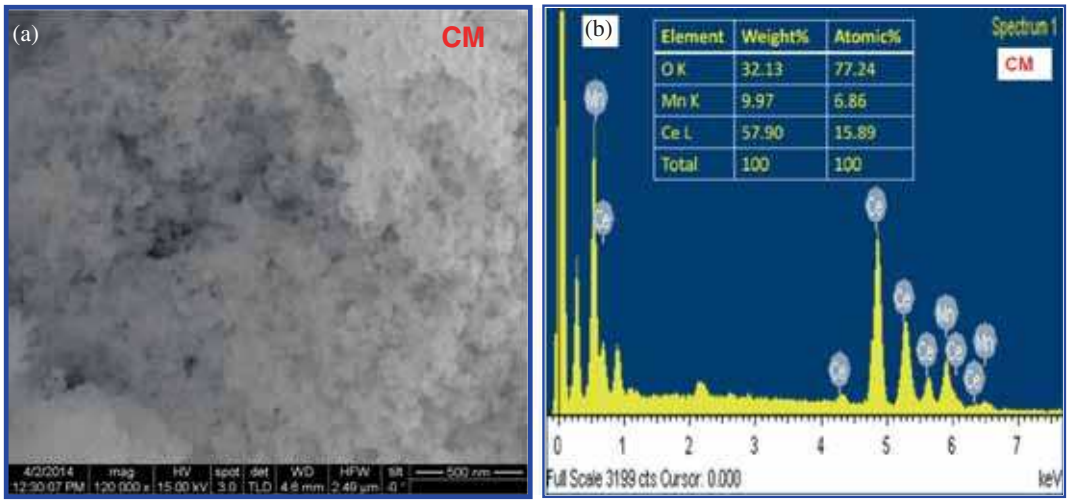

Figure 3. SEM-EDX images of (a, b) $Ce_{0.7}Mn_{0.3}O_{2-\delta}$(CM) sample calcined at 773 K.

crystallinity and a high stability of the nanoparticles. It is well-known that the HRTEM image of pure CeO_2 displayed the dominant (1 1 1) lattice fringes with the interplanar spacing of 0.312 nm.[16,30] In contrast, the doped CeO_2 samples showed little change and the distance was around 0.309 nm. Further, the absence of diffraction patterns and lattice fringes, corresponding to MO_x (M = Mn, Fe, Co) phases suggest that dopant ions are substituted in the CeO_2 lattice and forming the $Ce_{0.7}M_{0.3}O_{2-\delta}$ solid solution particles.

Raman spectroscopy was employed as a versatile analytical tool to characterize metal−oxygen (M−O) bonds as well as lattice defects in the investigated samples.[19] Figure 5 shows the Raman spectra of CM, CF, and CC samples calcined at 773 K along with the pure CeO_2. Generally, the pure CeO_2 shows two bands at ~464 and ~597 cm^{-1}. The prominent peak at ~464 cm^{-1} can be assigned to triply degenerate F_{2g} Raman active mode in the fluorite structure of ceria, which is the only one allowed in first order.[31] This F_{2g} peak originates from the symmetric breathing mode of the oxygen atoms which are located around Ce^{4+} ions. The comparatively weak band at ~597 cm^{-1} can be ascribed to the intrinsic oxygen vacancies due to the existence of Ce^{3+} ions.[31] Being related with oxygen mobility, the presence of oxygen vacancies are also important because of the possible role of these sites in certain oxidation reactions. Compared with pure ceria, the F_{2g} mode in all doped ceria samples shifts to a lower frequency and significantly broadens with imported dopant ions. It appears that CM sample presents the highest shift, whereas the CF and CC samples exhibit a little shift. The most probable interpretation for the shift and broadening of the peaks can be due to the significant modification of the M–O vibration frequency, which probably results from the presence of dopant ions in the fluorite lattice.[32] In addition to F_{2g} peak, all the CM, CF, and CC samples showed lower intensity peaks at ~590.7, 593.6, and 589.2 cm^{-1}, respectively. These peaks can be attributed to oxygen defects/vacancies (V_o) in the doped ceria structure.[30,31,33] It is well-known that the substitution of Ce^{4+} by the dopant ($M^{2+/3+}$) results in the creation of oxygen vacancies to compensate the effective negative charge produced in the CeO_2 lattice. To confirm the formation of oxygen vacancies in the doped ceria samples, the ratio between the peak areas of V_o (A_{Vo}) and F_{2g} (A_{F2g}) of the samples were calculated and listed in table 1. It can be seen from table 1 that the order of A_{Vo}/A_{F2g} values was CM > CF > CC > C. It was reported that the higher the A_{Vo}/A_{F2g} ratio, the higher the oxygen vacancies.[18] Therefore, the presence of dopants promoted formation of oxygen vacancies in the CeO_2 lattice. Surprisingly, the doped ceria samples also exhibited a few additional bands. For CM sample, the band at ~643 cm^{-1} can be assigned to a Mn–O–Mn stretching mode of crystalline Mn_3O_4 phase.[34] On the otherhand, two vibrational modes were observed for CF catalyst at ~218 and ~283 cm^{-1} and could be assigned to the presence of Fe_2O_3 oxide.[35] In the case of CC sample, a weak band at ~673 cm^{-1} can be assigned to the presence of Co_3O_4 oxide.[36] However, the Mn_3O_4, Fe_2O_3, and Co_3O_4 oxides were not detected by XRD analysis, which ensures the amorphous nature of dopant oxides dispersed on the ceria lattice. Therefore, the observed results indicate that transition metal doping distorts the crystal structure of cerium oxide through the formation of $Ce_{0.7}M_{0.3}O_{2-\delta}$ solid solutions and induces oxygen vacancies in the bulk of the ceria.

In order to find out the oxidation states of the elements present in the samples, the XPS experiments were performed. The Ce 3d XPS profile is shown in

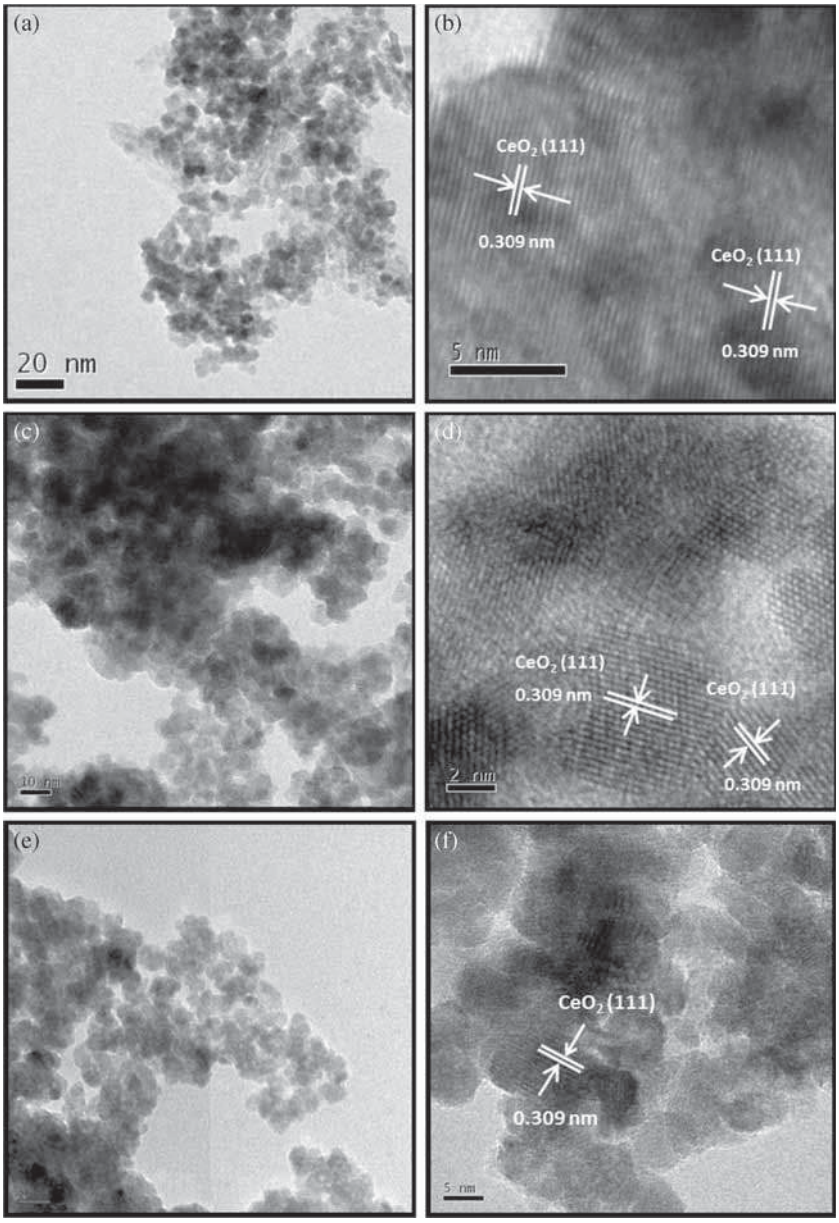

Figure 4. TEM (a, c, e) and HRTEM (b, d, f) images of $Ce_{0.7}Mn_{0.3}O_{2-\delta}$(CM), $Ce_{0.7}Fe_{0.3}O_{2-\delta}$ (CF), and $Ce_{0.7}Co_{0.3}O_{2-\delta}$(CC) samples calcined at 773 K.

figure 6. As can be seen from figure 6, the Ce 3d spectrum can be decomposed into eight components corresponding to four pairs of spin–orbit doublets.[37] The complex shape of the Ce 3d spectra mainly arises from the multiplet effect such as hybridization of Ce 4f orbitals with O 2p levels and final state, which are characteristic of CeO_2. The peaks labeled as "u" are due to Ce $3d_{3/2}$ spin-orbit states, and those labeled as "v" are due to the corresponding Ce $3d_{5/2}$ states. As shown in figure 6, six characteristic peaks u‴, u″, u and v‴, v″, v uniquely attributable to Ce^{4+} ions and those labeled as u′ and v′ can be attributed to Ce^{3+} ions.[37,38] These results confirm that both Ce^{4+} and Ce^{3+} ions are existing on the surface of the catalysts. Surprisingly, it was observed that the ratio of $Ce^{3+}/(Ce^{3+}+Ce^{4+})$ is changed in the doped ceria samples while compared to pure CeO_2. In order to verify this observation, the relative content of $Ce^{3+}/(Ce^{3+}+Ce^{4+})$ over various catalyst surfaces was calculated by peak fitting of Ce 3d XPS and the obtained results are listed in table 2. The order of Ce^{3+} concentration was CM > CF > CC > C. This observation can be due to the transformation of Ce species from Ce^{4+} to Ce^{3+} caused by the replacement of Ce^{4+} by dopant ions and forming more oxygen vacancies. The presence of oxygen vacancies concentration from XPS study is fairly supported by the Raman analysis. Further, the u‴ intensity (Ce^{4+}) of doped ceria samples shifted to lower energy side. This

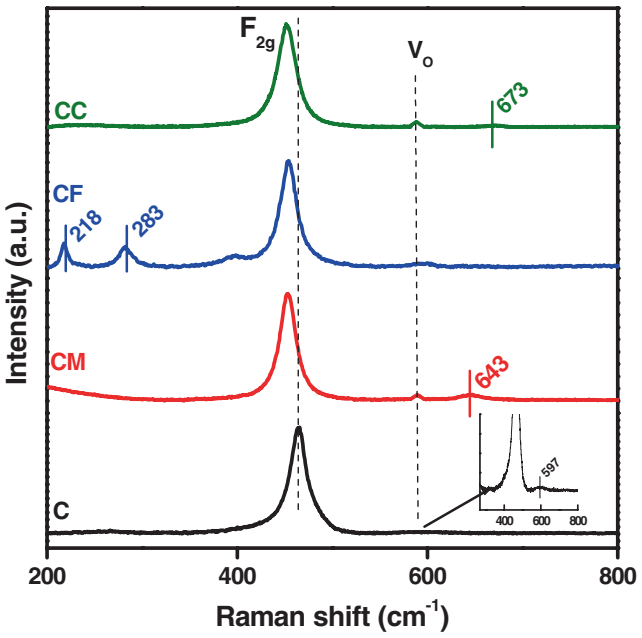

Figure 5. Raman spectra of pure CeO_2(C), $Ce_{0.7}Mn_{0.3}O_{2-\delta}$(CM), $Ce_{0.7}Fe_{0.3}O_{2-\delta}$ (CF), and $Ce_{0.7}Co_{0.3}O_{2-\delta}$(CC) samples calcined at 773 K.

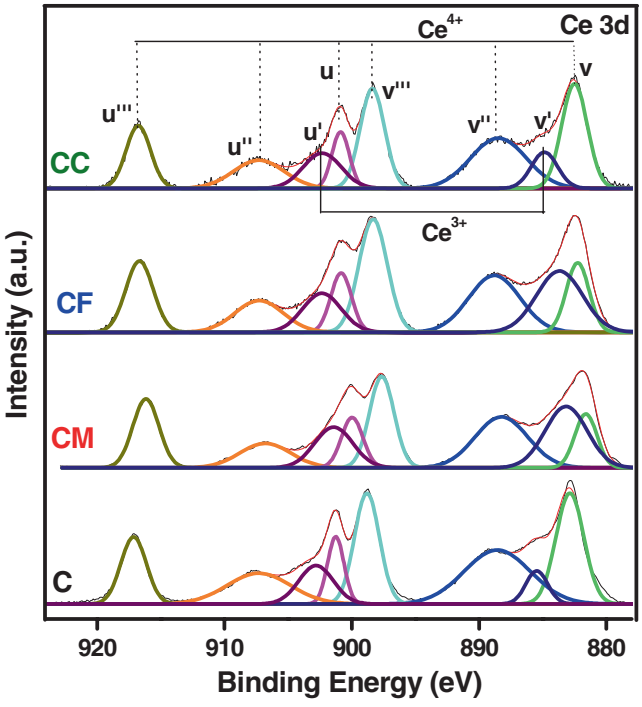

Figure 6. Ce 3d core level XPS spectra of pure CeO_2(C), $Ce_{0.7}Mn_{0.3}O_{-\delta}$ (CM), $Ce_{0.7}Fe_{0.3}O_{2-\delta}$ (CF), and $Ce_{0.7}Co_{0.3}O_{2-\delta}$ (CC) samples calcined at 773.

observation indicates that doping influences the chemical environment of pure CeO_2.[26] Based on these observations, the special redox couple Ce^{4+}/Ce^{3+}, in the form of CeO_2/Ce_2O_3, could easily generate labile oxygen vacancies and highly mobile oxygen species, which play an important role in the CO oxidation.[39,40] Besides, it was reported that the concentration of oxygen vacancies in the ceria are related to the particle size, thereby smaller nanoparticles posses a higher concentration of oxygen vacancies.[41] As the structure of doped ceria samples fabricated in this work consist of nanosized particles of fluorite structured ceria as building units which is evidenced from XRD, BET and TEM investigations, a high concentration of the oxygen vacancy can be expected. In particular, among all the samples, the CM sample had the smallest particle size from the above mentioned measurements as well as it has a maximum Ce^{3+} concentration as observed from XPS analysis.

The binding energies of Mn 2p, Fe 2p, Co 2p, and O 1s have been recorded for various catalysts and the results are shown in figure 7. Spectra of the Mn 2p region, depicted in figure 7a, exhibited two peaks located at ~641.4 and ~653.1 eV. The former peak arises from Mn $2p_{3/2}$, and the later peak can be due to Mn $2p_{1/2}$. The spin orbit splitting distance of these peaks is $\Delta E = 11.7$ eV. The observed binding energy value of Mn $2p_{3/2}$ at 641.4 eV indicates that Mn is existed in 2+ and 3+ oxidation states bonding with oxygen. Because the binding energy (BE) of Mn^{2+} and Mn^{3+} are very close to each other, a distinct identification of the oxidation states is not possible, which is consistent with the results of Machida *et al.* and Murugan *et al.*[42,43] The co-existence state of MnO–Mn_2O_3 can promote the catalytic oxidation of CO to CO_2 at low temperatures. Further, the measured binding energies of Mn ions are lower than those of pure MnO and Mn_2O_3, which indicates a strong interaction between manganese and cerium oxides.[44] As shown in figure 7b, the Fe 2p spectra shows characteristic of Fe $2p_{3/2}$ and Fe $2p_{1/2}$ peaks at binding energies of ~711.4 and ~724.7 eV, respectively. In addition to the above two peaks, two satellite peaks are also observed. These satellite peaks are clearly distinguishable and did not overlap either of the Fe $2p_{3/2}$ or Fe $2p_{1/2}$ peaks. The binding energy of Fe $2p_{3/2}$ at ~711.4 eV, the difference between Fe $2p_{3/2}$ and Fe $2p_{1/2}$ peaks (~13.3 eV), and the presence of two satellite peaks are characteristic of Fe 2+ and Fe 3+ states.[45,46] In addition, there appears to be another satellite peak at ~733.1 eV and it may be a satellite peak for Fe $2p_{1/2}$.[47] Figure 7c presents the Co 2p XPS spectra containing the well defined doublet peaks of Co $2p_{3/2}$ and Co $2p_{1/2}$. It was found that the binding energies of Co $2p_{3/2}$ and Co $2p_{1/2}$ peaks are around ~780.2 and ~795.3 eV, respectively. The observed Co $2p_{3/2}$ value is close to the value reported for CoO, indicating that cobalt can be present as Co^{+2} on the surface.[48] Usually, the splitting value of the doublet Co $2p_{3/2}$–Co $2p_{1/2}$

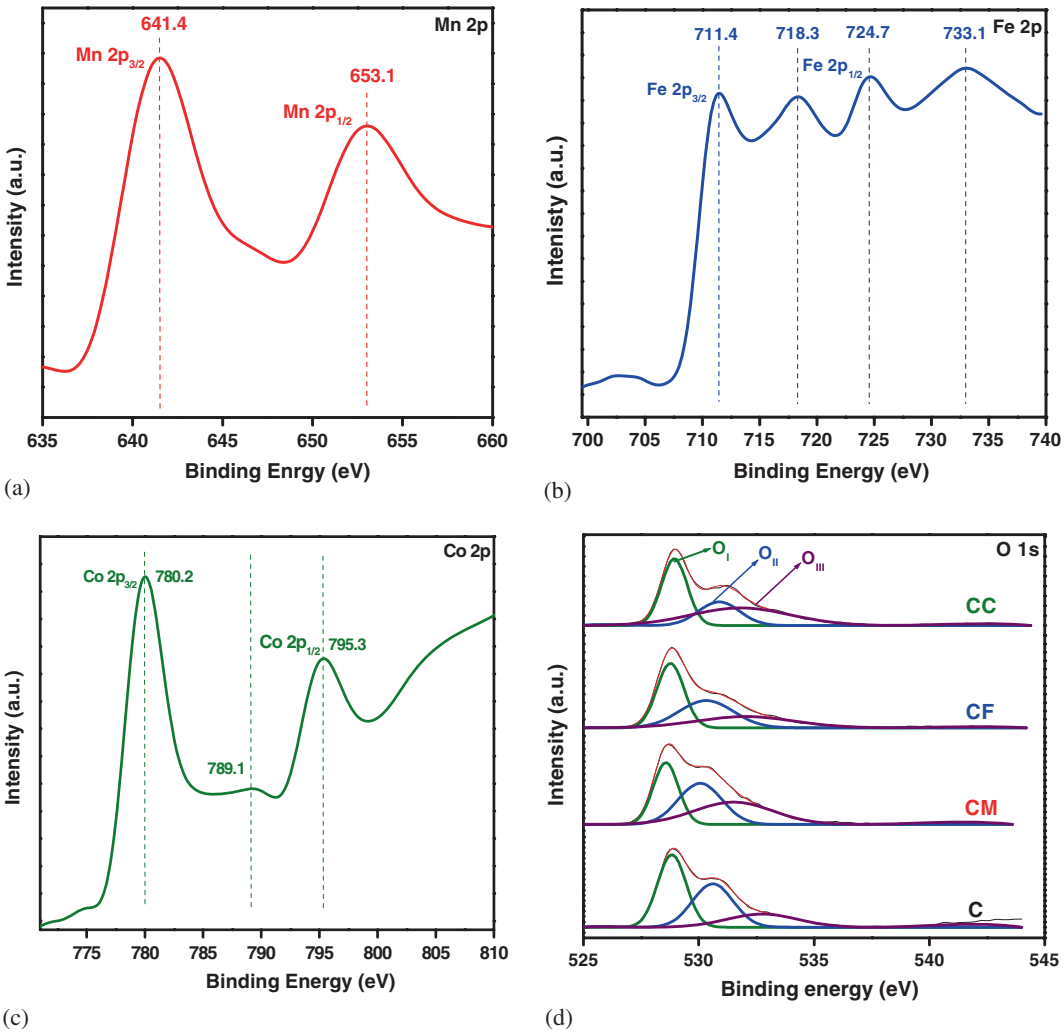

Figure 7. (a) Mn 2p; (b) Fe 2p; (c) Co 2p; and (d) O 1s spectra of $Ce_{0.7}Mn_{0.3}O_{2-\delta}$(CM), $Ce_{0.7}Fe_{0.3}O_{2-\delta}$ (CF), $Ce_{0.7}Co_{0.3}O_{2-\delta}$ (CC), and pure CeO_2(C) samples calcined at 773 K.

(ΔCo) allows discrimination between Co^{+2} and Co^{+3}. Indeed, a $\Delta Co = 16$ eV is reported for the high-spin Co^{+2}, while $\Delta Co = 15$ eV for the low-spin Co^{+3} ions.[49] The ΔCo is, in our case, of ~15.1 eV, which suggests the presence of Co^{+3} on the surface. The existence of the satellite peak at about ~789.1 eV is also correlated with the presence of Co^{2+} species. From these results, it can be concluded that cobalt ion is present in a mixed valence state on the surface, i.e. Co^{2+} and Co^{3+}.

The O 1s XPS spectra of all synthesized catalysts are analyzed in order to investigate the characteristics of surface oxygen species as shown in figure 7d. The O 1s spectra of catalysts are fitted with three peak contributions. The first peak at ~528.5–528.9 eV corresponds to lattice oxygen (O_I), the second peak at ~530.1–530.9 eV can be attributed to the defect oxides or surface hydroxyl groups (O_{II}), and the third peak at ~531.6–532.8 eV can be ascribed to carbonates and/or water molecules (O_{III}) with low coordination.[50] Compared to pure ceria, the O 1s core levels of O_I, O_{II} and O_{III} over all CM, CF, and CC samples shifted to lower values. The doping of lower valent cations (Mn, Fe, and Co) into the CeO_2 lattice generates excess negative charge, thereby shifting the O 1s binding energy to the lower binding energy side. Generally, the defect oxygen species (O_{II}) or surface hydroxyl groups are the most active oxygen and can play a vital role in the oxidation reactions.[51] The relative percentages of these different oxygen species are quantified based on the summation of peak areas and the results are listed in table 2. Obviously, the addition of Mn, Fe, and Co oxides results in more O_{II}% in comparison to pure CeO_2. Especially for the CM sample (37.08%), the proportion of O_{II} species is higher than that of CF, CC, and pure CeO_2, which means that it has richer surface active oxygen than the other samples. This result is in good accordance with the H_2-TPR measurements in which doped ceria samples exhibited a surface reduction peak

Table 2. Binding energies and surface atomic concentrations of pure CeO_2(C), $Ce_{0.7}Mn_{0.3}O_{2-\delta}$ (CM), $Ce_{0.7}Fe_{0.3}O_{2-\delta}$ (CF), and $Ce_{0.7}Co_{0.3}O_{2-\delta}$ (CC) samples calcined at 773 K.

Sample	$Ce^{3+}/Ce^{3+}+Ce^{4+}$ (%)	Ce 3d (u‴) (eV)	O 1s centre (eV)			Surface atomic concentration O/O_T(%)		
			O_I	O_{II}	O_{III}	O_I	O_{II}	O_{III}
C	27.58	917.13	528.9	530.8	532.8	41.82	32.27	25.91
CM	35.61	916.21	528.5	530.1	531.6	40.08	37.08	22.84
CF	32.75	916.87	528.7	530.4	532.1	43.25	34.44	22.31
CC	29.87	916.82	528.9	530.7	532.3	39.26	33.49	27.25

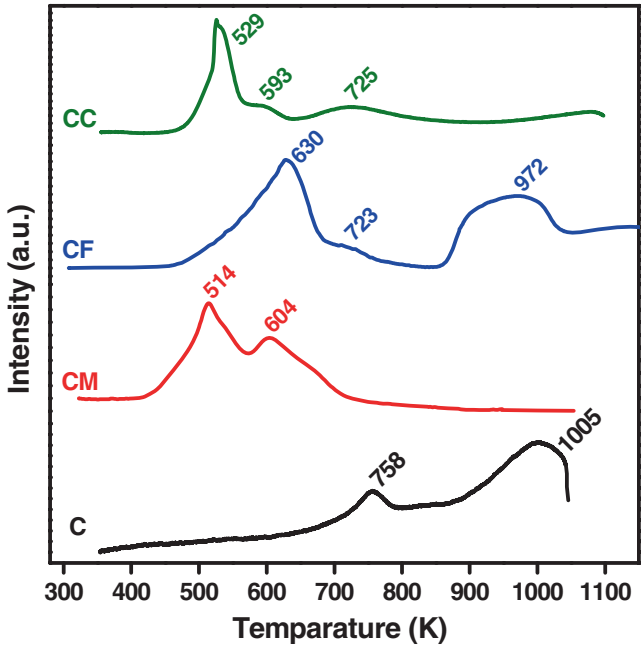

Figure 8. H_2-TPR spectra of pure CeO_2(C), $Ce_{0.7}Mn_{0.3}O_{2-\delta}$(CM), $Ce_{0.7}Fe_{0.3}O_{2-\delta}$ (CF), and $Ce_{0.7}Co_{0.3}O_{2-\delta}$ (CC) samples calcined at 773 K.

at lower temperature than pure ceria. It is well-known that the high O_{II} concentration always exhibits great influence on the catalytic activity for low-temperature CO oxidation.[36] This result may provide another reasonable explanation for the low-temperature activity of CM sample in the following CO activity tests.

The redox properties of the catalysts play an important role in catalytic oxidation reactions and the H_2-TPR is an effective method to obtain such information. The H_2-TPR profiles for pure CeO_2, CM, CF, and CC samples calcined at 773 K are shown in figure 8. There are two broad peaks at ~758 and 1005 K on the spectrum of pure ceria within the test temperature range. According to the literature,[10,52,53] the first peak around ~758 K can be ascribed to the reduction of surface Ce^{4+} to Ce^{3+} and the other peak at ~1005 K is generally corresponds to the reduction of bulk CeO_2. The reduction profiles of the CM, CF, and CC samples shifted to lower temperatures compared to pure ceria, indicating that the dopant ions could promote the reducibility of neighboring Ce ions and there is a synergistic interaction between Ce-O and M-O (M = Mn, Fe, and Co) oxides through the formation of $Ce_{0.7}M_{0.3}O_{2-\delta}$ solid solutions.[15] In particular, the surface reduction peak of pure ceria has changed significantly upon doping. This can be due to the weakly bounded oxygen atoms in Ce-O-M than in Ce-O-Ce. Further, it has been accepted that the higher surface area of the mixed oxides in comparison to pure ceria could also promote its reduction. This fact can be further confirmed from the appearance of broad lattice diffraction peaks of doped-CeO_2 in the XRD patterns (figure 1a). For CM sample, a major peak at ~514 K and a weak peak at 604 K were found. Zou *et al*. also reported very similar TPR profile for Mn doped CeO_2 catalyst prepared by a co-precipitation method.[27] The low temperature reduction peak could be assigned to the reduction of MnO_2/Mn_2O_3 to Mn_3O_4, and the high-temperature reduction peak corresponds to the combined reduction of Mn_3O_4 to MnO and surface oxygen removal of ceria.[54] As shown in figure 8, three reduction peaks were detected in CF and CC samples. However, the CC sample showed the reduction peaks at lower temperature than CF sample. Reduction peaks at ~630, 723, and 972 K are found for CF sample. According to the literature reports, they can be ascribed to the reduction of $Fe_2O_3 \rightarrow Fe_3O_4$, the consumption of surface CeO_2 and overlapping of the reduction of $Fe_3O_4 \rightarrow$ FeO, and the release of the bulk oxygen of ceria as well as overlapping of the FeO $\rightarrow$ Fe^0, respectively.[55,56] A similar curve was observed for CC sample with reduction peaks at ~529, 593, and 725 K. The peaks at ~529 and 593 K can be assigned to the reduction of Co_3O_4 interacting with CeO_2 to CoO and the subsequent reduction of CoO to metallic Co. The third peak at high temperature can be attributed to the reduction of subsurface oxygen species of ceria.[20,22] From the above results, it can be concluded that the reducibility of the pure ceria, mainly for the surface reduction step, is strongly enhanced by dopants incorporation that favours oxygen mobility. It is widely accepted that high mobility of oxygen in the surface and bulk gives an important contribution to the CO oxidation activity.

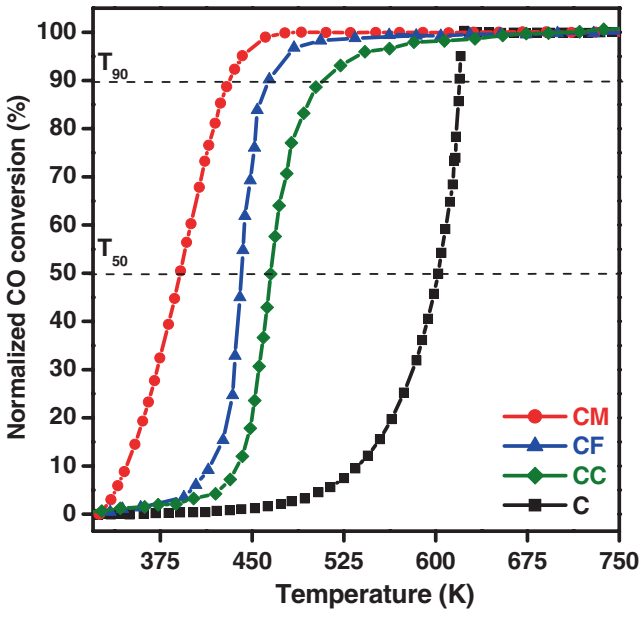

Figure 9. Conversion of CO (%) versus temperature (K) for pure CeO_2 (C), $Ce_{0.7}Mn_{0.3}O_{2-\delta}$(CM), $Ce_{0.7}Fe_{0.3}O_{2-\delta}$ (CF), and $Ce_{0.7}Co_{0.3}O_{2-\delta}$ (CC) samples calcined at 773 K.

3.2 *Activity studies*

The catalytic oxidation of CO on mixed metal oxide surfaces is one of the major current research topics due to its relatively simple mechanism. The CO oxidation reaction can be used as a cornerstone to establish a model for more complex catalytic reactions on surfaces. It is well-known that ceria is very useful for the catalytic oxidation of CO due to the special oxygen storage and release properties.[8] In order to improve the catalytic CO oxidation performance, the doping of transition metals such as Mn, Fe, and Co into ceria lattice is very important. The catalytic performance of different metals (Mn, Fe, Co) doped ceria solid solutions and pure CeO_2 for CO oxidation in the temperature range of 300–750 K is shown in figure 9. As observed from figure 9, the catalytic activity of all the samples increased as the reaction temperature increases. It is also clear from the figure that CM sample exhibited high activity compared to all other investigated catalysts. The 100% conversion of CO to CO_2 can be achieved at temperatures lower than ~525 K for all $Ce_{0.7}Mn_{0.3}O_{2-\delta}$, $Ce_{0.7}Fe_{0.3}O_{2-\delta}$, and $Ce_{0.7}Co_{0.3}O_{2-\delta}$ solid solutions. On the other hand, a high temperature is required for 100% CO conversion for bare CeO_2 (> 600 K). From the figure, the light–off temperature curves T_{50}(50% CO conversion temperature) and T_{90} (90% CO conversion temperature) of CO oxidation clearly explain that the transition metals doping into ceria strongly influences the catalytic activity of the investigated samples. The catalytic activity for CO oxidation followed the order: CM > CF > CC > C. The superior performance of mixed oxides compared to pure ceria at lower temperatures could be attributed to the strong synergistic interaction between transition metal ions and CeO_2. To confirm the synergistic interaction, the CO oxidation performance of CeO_2–MnO_x mixed oxide is compared with that of pure CeO_2 and MnO_x as shown in figure S2 (supporting information). It was found that the Mn doped CeO_2 reduced the T_{50} value when compared to individual oxides. Therefore, it can be concluded that the introduction of transition metals into ceria lattice, the Ce–O and M–O bonds are weakened through the formation of the $Ce_{0.7}M_{0.3}O_{2-\delta}$ solid solution, thereby reducing the oxygen vacancy formation energy and enhancing the reactivity of the surface. Further, the enhancement of reactivity could be explained that the presence of surface oxygen vacancies, thus the chemisorbed CO migrates to the periphery of the CeO_2–MO_x interface and reacts with the activated O^{2-} and generates CO_2. As observed from the results of BET surface area in table 1, CM catalyst has higher surface area than that of CF and CC samples, which leads to the increase of surface adsorbed oxygen. It is well established that the surface adsorbed oxygen is beneficial to the catalytic oxidation of CO at lower temparatures.[36] H_2-TPR results disclosed that CM catalyst shows the superior redox properties (particularly surface reduction) compared to all other investigated catalysts and the order was CM > CF > CC > C. Similarly, the T_{50} and T_{90} values of the catalysts are also followed the same trend as shown in table S3 (supporting information), suggesting that the CO oxidation performance could be correlated with the facile redox nature of the mixed oxides as well. Summing up, the enhanced reducibility of $Ce_{0.7}Mn_{0.3}O_{2-\delta}$ solid solution in conjunction with its high surface area can be considered crucial towards CO activity. Further, from the XPS results, the Mn element on the surface of CeO_2–MnO_x catalyst is mainly as Mn^{2+}/Mn^{3+}, which exhibit good ability to activate oxygen. Therefore, it is clear that the Mn element in CeO_2–MnO_x mixed oxides can activate oxygen and the Ce^{4+} in that can absorb and activate CO. Therefore, CO oxidation reaction over Mn^{3+}–O–Ce^{4+} species probably follows the interfacial reaction mechanism, in which CO adsorbed on Ce^{4+} reacts with O adsorbed on adjacent Mn^{3+} to form CO_2. Accordingly, the CeO_2–MnO_x catalyst possessed the largest specific surface area, more manganese species with higher oxidation states on the catalyst surface, and the best reducibility, which resulted in its best catalytic activity. Moreover, the CO conversion of all samples is stable even at higher temperature, which shows the higher thermal stability of all the doped ceria samples. Compared to other doped-ceria systems such as Sn, Zr

and Hf, the $Ce_{0.7}M_{0.3}O_{2-\delta}$ solid solutions prepared in this work showed high activity in CO oxidation, which confer them great potential as important materials for oxidation reactions.[57,58]

4. Conclusions

In summary, the transition metal-doped CeO_2 catalysts ($Ce_{0.7}M_{0.3}O_{2-\delta}$, M = Mn, Fe, Co) were successfully prepared by simple and facile co-precipitation method. The structural characteristics and CO oxidation activity of these catalysts have been systematically investigated by XRD, ICP-OES, BET surface area, SEM-EDX, TEM and HRTEM, Raman, XPS, and H_2-TPR techniques. The XRD results demonstrated that all the samples can be indexed to the cubic fluorite structured ceria. The absence of the peaks corresponding to MO_x indicates the formation of $Ce_{0.7}M_{0.3}O_{2-\delta}$ (M = Mn, Fe, and Co) solid solutions where an interstitial substitution of dopant ions in the Ce sites takes place. A clear spherical morphology of $Ce_{0.7}M_{0.3}O_{2-\delta}$ solid solution nanoparticles with uniform particle size in the range of ∼8–16 nm was revealed by TEM-HRTEM analysis. Raman spectra indicated the cubic fluorite structure of ceria and the existence of oxygen vacancies, and displacement of oxygen ions from their normal lattice positions in the ceria-based mixed oxides. A high percentage of Ce^{3+} valence state was determined by XPS for the $Ce_{0.7}Mn_{0.3}O_{2-\delta}$ sample. The formation of surface adsorbed oxygen depends on the nature of the dopants, especially doping with Mn highly enhances the formation of surface absorbed oxygen. $Ce_{0.7}Fe_{0.3}O_{2-\delta}$ and $Ce_{0.7}Co_{0.3}O_{2-\delta}$ solid solutions also presented more surface absorbed oxygen than pure CeO_2. From H_2-TPR, it is clear that $Ce_{0.7}Mn_{0.3}O_{2-\delta}$ sample showed enhanced surface reduction at lower temperatures, indicating a high mobility of oxygen ions in this sample. Particularly, the $Ce_{0.7}Mn_{0.3}O_{2-\delta}$ solid solution exhibits the superior activity towards CO oxidation reaction compared to $Ce_{0.7}Fe_{0.3}O_{2-\delta}$ and $Ce_{0.7}Co_{0.3}O_{2-\delta}$ solid solutions. The ability to release a substantial amount of oxygen at relatively low temperatures makes $Ce_{0.7}Mn_{0.3}O_{2-\delta}$ solid solution a potential material for catalytic applications. This research may be suggestive for the synthesis of Ce-based metal oxide systems for various catalytic oxidation reactions at lower cost.

Supplementary Information

Detailed information about the Williamson-Holl (We-H) plots, CO oxidation profile, calculation of crystallite size using Debye-Scherrer equation, chemical composition by ICP-OES analysis, surface reduction temperatures, and characteristic temperatures of CO oxidation of all the investigated catalysts calcined at 773 K are available at www.ias.ac.in/chemsci.

Acknowledgements

We greatly acknowledge Prof. Dr. W. Grünert, Ruhr University Bochum, Germany for providing CO oxidation results. PV thanks Council of Scientific and Industrial Research (CSIR), New Delhi for the Senior Research Fellowship. DJ thanks IICT-RMIT Joint Research Centre for the award of Junior Research Fellowship. Financial support was received from the Department of Science and Technology, New Delhi, under SERB Scheme (SB/S1/PC-106/2012).

References

1. Vecchietti J, Collins S, Delgado J J, Małecka M, Rio E D, Chen X, Bernal S and Bonivardi A 2011 *Top. Catal.* **54** 201
2. Xiaodong Z, Zhenping Q, Fangli Y and Yi W 2013 *Chin. J. Catal.* **34** 1277
3. Royer S and Duprez D 2011 *Chem. Cat. Chem.* **3** 24
4. Biabani-Ravandi A and Rezaei M 2012 *Chem. Eng. J.* **184** 141
5. Manasilp A and Gulari E 2002 *Appl. Catal., B* **37** 17
6. Falcón H, Martinez-Lope M J, Alonso J A and Fierro J L G 2000 *Appl. Catal., B* **26** 131
7. Rao K N, Bharali P, Thrimurthulu G and Reddy B M 2010 *Catal. Commun.* **11** 863
8. KasÏpar J, Fornasiero P and Graziani M 1999 *Catal. Today* **50** 285
9. Katta L, Sudarsanam P, Thrimurthulu G and Reddy B M 2010 *Appl. Catal. B* **101** 101
10. Rao G R and Mishra B G 2003 *Bull. Catal. Soc. India* **2** 122
11. Mai H-X, Sun L-D, Zhang Y-W, Si R, Feng W, Zhang H-P, Liu H-C and Yan C-H 2005 *J. Phys. Chem. B* **109** 24380
12. Meher S K and Ranga Rao G 2012 *J. Colloid Interface Sci.* **373** 46
13. Kehoe A B, Scanlon D O and Watson G W 2011 *Chem. Mater.* **23** 4464
14. Saqer S M, Kondarides D I and Verykios X E 2011 *Appl. Catal. B* **103** 275
15. Yeqin S, Ying Z, Hanfeng L, Zekai Z and Yinfei C 2013 *Chin. J. Catal.* **34** 567
16. Mousavi S M, Niaei A, Gómez M J, Salari D, Panahi P N and Abaladejo-Fuentes V 2014 *Mater. Chem. Phys.* **143** 921
17. Tang C-W, Wang C-B and Chien S-H 2009 *Catal. Lett.* **131** 76
18. Yu D, Liu Y and Wu Z 2010 *Catal. Commun.* **11** 788
19. Bharali P, Saikia P, Katta L and Reddy B M 2013 *J. Ind. Eng. Chem.* **19** 327
20. Wang J, Shen M, Wang J, Gao J, Ma J and Liu S 2011 *Catal. Today* **175** 65

21. Tang Y, Qiao H, Wang H and Tao P 2013 *J. Mater. Chem. A* **1** 12512
22. Luo J-Y, Meng M, Zha Y-Q and Guo L-H 2008 *J. Phys. Chem. C* **112** 8694
23. Kongzhai L, Hua W, Yonggang W and Mingchun L 2008 *J. Rare Earths* **26** 245
24. Zhou G, Shah P R and Gorte R J 2008 *Catal. Lett.* **120** 191
25. Choudhury B and Choudhury A 2012 *Mater. Chem. Phys.* **131** 666
26. Sudarsanam P, Mallesham B, Durgasri D N and Reddy B M 2014 *RSC Adv.* **4** 11322
27. Zou Z-Q, Meng M and Zha Y-Q 2010 *J. Phys. Chem. C* **114** 468
28. Ertl G, Knoezinger H, Schuth F and Weitkmp J 2008 In *Hand book of heterogeneous catalyst* 2nd ed. (Weinheim: Wiley-VcH) Vol. 2 p.728
29. Channei D, Inceesungvorn B, Wetchakun N, Phanichphant S, Nakaruk A, Koshy P and Sorrell C C 2013 *Ceram. Int.* **39** 3129
30. Yu Y, Zhong L, Ding J, Cai W and Zhong Q 2015 *RSC Adv.* **5** 23193
31. Zhang X, Wei J, Yang H, Liu X, Liu W, Zhang C and Yang Y 2013 *Eur. J. Inorg. Chem.* 4443
32. Li K, Wang H, Wei Y and Yan D 2011 *Int. J. Hydrogen Energy* **36** 3471
33. Qiao D, Lu G, Liu X, Guo Y, Wang Y and Guo Y 2011 *J. Mater. Sci.* **46** 3500
34. Fazio B, Spadaro L, Trunfio G, Negro J and Arena F 2011 *J. Raman Spectrosc.* **42** 1583
35. Zhu X, Wei Y, Wang H and Li K 4492 *Int. J. Hydrogen Energy* **38** 2103
36. Lou Y, Wang L, Zhang Y, Zhao Z, Zhang Z, Lu G and Guo Y 2011 *Catal. Today* **175** 610
37. Yao X, Tang C, Ji Z, Dai Y, Cao Y, Gao F, Dong L and Chen Y 2013 *Catal. Sci. Technol.* **3** 668
38. Zhang Y-W, Si R, Liao C-S and Yan C-H 2003 *J. Phys. Chem. B* **107** 10159
39. Wu Z, Jin R, Liu Y and Wang H 2008 *Catal. Commun.* **9** 2217
40. Zhang F, Wang P, Koberstein J, Khalid S and Chan S-W 2004 *Surf. Sci.* **563** 74
41. Santra C, Rahman S, Bojja S, James O O, Sen D, Maity S, Mohanty A K, Mazumder S and Chowdhury B 2013 *Catal. Sci. Technol.* **3** 360
42. Machida M, Uto M, Kurogi D and Kijima T 2000 *Chem. Mater.* **12** 3158
43. Murugan B and Ramaswamy A V 2008 *J. Phys. Chem. C* **112** 20429
44. Nesbitt H W and Banerjee D 1998 *Am. Mineral.* **83** 305
45. Zhang Z, Han D, Wei S and Zhang Y 2010 *J. Catal.* **276** 16
46. Venkataswamy P, Jampaiah D, Rao K N and Reddy B M 2014 *Appl. Catal., A* **488** 1
47. Yamashita T and Hayes P 2008 *Appl. Surf. Sci.* **254** 2441
48. Li J-G, Büchel R, Isobe M, Mori T and Ishigaki T 2009 *J. Phys. Chem. C* **113** 8009
49. Norman C and Leach C 2011 *J. Membr. Sci.* **382** 158
50. Li K, Wang H, Wei Y and Yan D 2011 *Chem. Eng. J.* **173** 574
51. Ma C, Mu Z, He C, Li P, Li J and Hao Z 2011 *J. Environ. Sci.* **23** 2078
52. Chen L, Li J and Ge M 2009 *J. Phys. Chem. C* **113** 21177
53. Durgasri D N, Vinodkumar T and Reddy B M 2014 *J. Chem. Sci.* **126** 429
54. Fraccari E P, D'Alessandro O, Sambeth J, Baronetti G and Mariño F 2014 *Fuel Process. Technol.* **119** 67
55. Li K, Wang H, Wei Y and Yan D 2010 *Chem. Eng. J.* **156** 512
56. Laguna O H, Sarria F R, Centeno M A and Odriozola J A 2010 *J. Catal.* **276** 360
57. Ayastuy J L, Iglesias-González A and Gutiérrez-Ortiz M A 2014 *Chem. Eng. J.* **244** 372
58. Reddy B M, Bharali P, Saikia P, Park S-E, van den Berg M W E, Muhler M and Grünert W 2008 *J. Phys. Chem. C* **112** 11729